Control of C3N4 and C4N3 carbon nitride nanosheets' electronic and magnetic properties through embedded atoms

PCCP
Physical Chemistry Chemical Physics

Accepted Manuscript

This article can be cited before page numbers have been issued, to do this please use: A. Bafekry, C. Stampfl, B. Akgenc and M. Ghergherehchi, *Phys. Chem. Chem. Phys.*, 2020, DOI: 10.1039/C9CP06031F.

View Article Online
DOI: 10.1039/C9CP06031F

Control of C_3N_4 and C_4N_3 carbon nitride nanosheets' electronic and magnetic properties through embedded atoms

Asadollah Bafekry,[*,†‡] Catherine Stampfl,[¶] Berna Akgenc,[§] and Mitra Ghergherehchi[‖]

[†]*Department of Physics, University of Guilan, 41335-1914, Rasht, Iran,* [‡]*Department of Physics, University of Antwerp, Groenenborgerlaan 171, B-2020 Antwerp, Belgium.,* [¶] *School of Physics, The University of Sydney, New South Wales 2006, Australia,* [§] *Department of Physics, Kirklareli University, Kirklareli, Turkey, and* [‖]*College of Electronic and Electrical Engineering, Sungkyun kwan University, Suwon, Korea*

E-mail: Asadollah.Bafekry@uantwerpen.be

Abstract

In the present work, the effect of various embedded atom impurities on tuning electronic and magnetic properties of C_3N_4 and C_4N_3 nanosheets have been studied using first-principles calculations. Our calculations show that C_3N_4 is a semiconductor and it exhibits extraordinary electronic properties such as dilute-magnetic semiconductor (with H, F, Cl, Be, V, Fe and Co); metal (with N, P, Mg and Ca), half-metal (with Li, Na, K, Al, Sc, Cr, Mn, and Cu) and

[*]To whom correspondence should be addressed
[†]Department of Physics, University of Guilan, 41335-1914, Rasht, Iran
[‡]Department of Physics, University of Antwerp, Groenenborgerlaan 171, B-2020 Antwerp, Belgium.
[¶]School of Physics, The University of Sydney, New South Wales 2006, Australia
[§] Department of Physics, Kirklareli University, Kirklareli, Turkey
[‖] College of Electronic and Electrical Engineering, Sungkyun kwan University, Suwon, Korea

View Article Online
DOI: 10.1039/C9CP06031F

semiconductor (with O, S, B, C, Si, Ti, Ni and Zn) with the band gaps in the range of 0.3-2.0 eV depending on the species of embedded atom. The calculated electronic properties reveal that C_4N_3 is a half-metal and it retains half-metallic character with embedded H, O, S, F, B, N, P, Be, Mg, Al, Sc, V, Fe, Ni and Zn atoms. The substitution of Cl, C, Cr and Mn atoms create ferromagnetic-metal character in the C_4N_3 nanosheet, embedded Co and Cu atoms exhibit a dilute-magnetic semiconductor nature, and embedded Ti atoms result in the system becomes a semiconductor. Therefore, our results reveal the fact that the band gap and magnetism can be modified or induced by various atom impurities, thus, offering effective possibilities to tune the electronic and magnetic properties of C_3N_4 and C_4N_3 nanosheets.

Introduction

Two-dimensional carbon nitride (2D-CN) monolayers and their 2D allotropes have recently been added to the large subgroup of 2D materials.[1–3] Since the successful synthesis of 2D-carbon nitrides,[4] 2D-CN have received significant recent interest. The 2D-CN monolayers have outstanding properties like graphene, where the sp^2-hybridization stems from the strong C-C bonds. Surface engineerin of these CN nanosheets enable the band gap to be tailored indicating they may have potential applications in both energy and environmental related areas, such as photocatalysis for water splitting and hydrogen evolution. Because the atomic and electronic structure enables covalent bonding, 2D-CN monolayers exhibit novel mechanical, optical, electronic and thermal properties.[5–8] Although several 2D-CN and their 2D allotropes can be experimentally produced, some of them have just been theoretically examined[9–12] Theoretical studies for C_4N_3 have predicted a half-metallic nature as well as metal-free magnetism in both C_4N_3 and nanotubes[13–17] which could be useful in spintronics devices. C_4N_3 also has potential for metal-free photocatalyst applications by manipulating its electronic band structure.

Over the past decade, tunable electronic and magnetic engineering of two-dimensional (2D) materials have attracted significant attention due to excellent properties such as new quantum states of matter,[18–21] topological insulators,[22] tuning electronic properties[23,24] novel spontaneous polar-

View Article Online
DOI: 10.1039/C9CP06031F

ization,[25] high mobility, high conductivity and high mechanical strength as well as long spin diffusion length for next-generation device applications.[26,27] Various approaches (such as introducing defect, applying electric fields/strain, functionalization, and application of embedded of atoms (substitutional/adsorption) have been explored to tune the electronic and magnetic properties of carbon nitride monolayers.[28–45] Theoretical calculations have investigated how the electronic and magnetic properties of 2D nanosheets change with embedded atoms.[46–55] Much effort has been devoted to searching new 2D nanosheets with tailored electronic and magnetic properties, which could be applied in technological devices such as nanoelectronics, spintronics, energy storage and catalysis.[56–73]

In this work, employing density functional theory, we systematically study the structural, electronic, and magnetic properties of embedded H, O, S, F, Cl, B, C, N, Si, P, Li, Na, K, Be, Mg, Ca, Al, Sc, Ti, V, Cr, Mn, Fe, Co, Ni and Zn atoms in the holey site of C_3N_4 and C_4N_3 nanosheets, and their pristine forms. Our results reveal that the embedded atoms significantly modify the electronic and magnetic properties. The findings highlight that pristine C_3N_4 and C_4N_3 nanosheets and those with embedded atoms in the holey sites result in various electronic behaviors including metal (M), half-metal (HM), ferromagnetic-metal (FM), dilute-magnetic semiconductor (DM-SC) and semiconductor (SC). The present results will provide a guide for future theoretical and experimental studies.

Computational Methodology

The density functional theory calculations were performed using the generalized gradient approximation for the exchange-correlation functional as proposed by Perdew-Burke-Ernzerhof (GGA-PBE),[74] along with norm-conserving pseudopotentials[75] as implemented in the OpenMX package. Following the convergence tests, the energy cutoff was selected to be 300 Ry as the plane-wave basis set. The wave functions are described using the linear combination of multiple pseudoatomic orbitals (LCPAOs) which is suitable for the calculation of large-scale electronic properties.[76,77]

View Article Online
DOI: 10.1039/C9CP06031F

The integrations are performed using a **k**-point mesh of $23 \times 23 \times 1$ with the Monkhorst-Pack scheme for the primitive unit cell.[78] 2D-CN was modeled with a vacuum region of about 20 Å to avoid interaction between neighboring slabs. The ground state structures were obtained by using a quasi-Newton algorithm. The ground state geometric structures were relaxed until the residual forces on the atoms were smaller than 1 meV/Å. The Tersoff-Hamann theory was used to obtain the scanning tunneling microscopy (STM) images implemented in the OpenMX package.[79] WSxM software was used in post-processing to plot the STM images, which assume a bias of +2.0 V.[80] The charge transfer analyses were performed by using the Mulliken charge analysis.[81]

Pristine C_3N_4 and C_4N_3 nanosheets

2D-CN can be formed in many allotropes because of its ability to exist in different hybridization with C and N atoms. In this study, we have focused C_3N_4 and C_4N_3 nanosheets. Fig. 1(a) shows the optimized crystal structures with lattice parameters of pristine C_3N_4 nanosheets. As seen in Fig. 1(a), primitive cell of C_3N_4 consists of three C and four N atoms. The lattice constant of the optimized C_3N_4 is calculated to be 4.74 Å. The bond distances of C-N atoms are found 1.32 and 1.44 Å for different types of the bonds. The bond angle of N-C-N is 117.4° and C_3N_4 exhibits a completely flat structure which is consistent with previous reports.[82] The lattice constant of the C_4N_3 nanosheet is calculated to be 4.81 Å. As shown in in Fig. 1(e), there are two inequivalent bond lengths of C-C and C-N of 1.42 and 1.34 Å, respectively. The bond angle of N-C-N of C_4N_3 is calculated as 120°. To gain understanding into the bond character of the pristine material, the total charge density and the charge density difference are presented in Figs. 1(a) and Figs. 1(e), respectively. Depletion and accumulation of electron density is indicated by the yellow and blue regions, respectively. According to our results, the C atoms are positively charged, whereas the N atoms are negatively charged, resulting in a strong bond character in the formed C-N bonds. The simulated STM images of C_3N_4 and C_4N_3 are shown in Figs. 1(b) and Figs. 1(f), respectively. The STM images are overlaid with their corresponding atomic structures, where brown and light blue

View Article Online
DOI: 10.1039/C9CP06031F

balls represent C and N atoms, respectively. From the STM images can be further be seen that the atoms in the bonds around C atom sites possess the brightest spots.

Our calculation show that C_3N_4 is a direct semiconductor with a band gap of 1.45 eV, where the valence band maximum (VBM) and the conduction band minimum (CBM) are located at the Γ point in the BZ (see Fig. 1(c)). This result agrees with a previous report,[9,10] suggestng that this material could be applicable for applications in nanoelectronics and optoelectronics. C_4N_3 is found to be exhibit half-metallic behavior with a gap of ~ 2.21 eV in the majority-spin ($\uparrow$) channel. the magnetic moment is calcualted to be 1 μ_B (see Fig. 1(g)), which is in agreement with previous calculations.[12–14] The half-metallic behavior could play key role in spintronic applications. Such half-metallicity may be understood by the fact that the pair of electrons in the bond (occupying a C-N bonding orbital) is broken after introduction of a hole at the substitutional N site. The calculated density of states (DOS) and partial (PDOS) of C_3N_4 show that the N-$s, p_{x,y}$ orbitals have a significant contribution in the VBM, while N/C-p_z orbitals are prominent in the CBM (Fig. 1(d)). The symmetric DOS indicates that C_3N_4 is a nonmagnetic semiconducting material. The valence band maximum consists of the lone pair orbitals on the two-coordinated N atoms of the triazine rings, and the conduction band minimum can is formed by p_z contributions on C and N atoms. For C_4N_3, a close examination of the VBM indicates that it is composed mainly of contributions from the planar C-p_z with N-$p_{x,y}$ orbitals in the majority $\uparrow$ spin channel and the CBM originates predominantly from N-$p_{x,y}$ orbitals in minority $\downarrow$ spin channel. The magnetic moment, and creation of the half-metallic behavior of C_4N_3, is mainly attributed to the N-$p_{x,y}$ orbitals near the E_F (see Fig. 1(h)). Thus, the charge transport is dominated by the spin-down electron, and the current flow in such a system should be fully spin-polarized, i.e., half-metallicity. Additionally, close examination of the top of the valence band (see Fig. 1(h)) indicates that the main contributions are from the planar p_x and p_y atomic orbitals. The difference spin density of C_4N_3 is also shown in the inset of Fig. 1(h). We can see that the magnetic moments are localized around the N atoms of C_4N_3.

View Article Online
DOI: 10.1039/C9CP06031F

Effect of embedded atoms

It is well known that embedded atoms can dramatically affect the structural, electronic, and magnetic properties of 2D materials. The affect of various embedded atoms on the electronic and magnetic properties of pristine C_3N_4 and C_4N_3 nanosheets are demonstrated in this study. A schematic view of the embedded atom into the holey site of C_3N_4 and C_4N_3 nanosheets are shown in Fig. 2(a). Hereafter, embedded atoms into C_3N_4 and C_4N_3 are labeled as atom-C_3N_4 and atom-C_4N_3, respectively. For instance, an embedded H atom into C_3N_4 is labeled as H-C_3N_4. The height and bond lengths for different species of embedded atoms (relative to the plane of the surface) into holey site of C_3N_4 and C_4N_3 are given in Figs. 2(b) and Figs. 2(c) in the same panel, respectively. In addition, the band gaps and magnetic moments of different embedded atoms are shown in Figs. 2(d-f). The corresponding calculated ground-state structural, electronic and magnetic parameters of the embedd atom systems are listed in Table 1. This includes the bond length between embedded-atom and its nearest neighbor atom (d_{AN}), the height of adatom from the C_3N_4 and C_4N_3 planes (h), the electronic state (ES), as specified as metal (M), half-metal (HM), ferromagnetic-metal (FM), semiconductor (SC), and dilute-magnetic semiconductor (DM-SC), the charge transfer (ΔQ) between embedding atom and C_3N_4 and C_4N_3 nanosheets, the magnetic moment per supercell $M_{tot}(\mu_B)$, and the initial magnetic moment of the atoms $M_{ISO}(\mu_B)$. The values in parentheses are the corresponding values for the C_4N_3 nanosheet.

Embedded H, O, S, F, Cl, B, C, Si, N and P atoms

The optimized top, side and perspective views of the structures of H, O, S, F, Cl, B, C, Si, N, and P embedded atoms into the holey site of C_3N_4 and C_4N_3 are shown in Fig. 3(a) and Fig. 3(b), respectively. We find that upon adsorption of the embedded atoms, the 2D planar structure are distorted. The H, O, and S atoms interact through sp^2-hybridization and form one σ bond to neighboring N atoms. It can be noticed that H, O, and S atoms induce a notable structural deformation perpendicular to the nanosheet surfaces and the bond lengths of H, O, and S are found

View Article Online
DOI: 10.1039/C9CP04031F

in the range of 1.34-1.54 Å. We also see that F and Cl are not bonded to host N atoms of C_3N_4 while they strongly bond to neighboring N atom in C_4N_3. The bond lengths of F and Cl atoms with their nearest neighboring N atom are 1.08 Å, and the C-C_H-H bond angle is 116°, and there is no distortion out of the plane. The F-C bond lengths are 1.58 and 1.71 Å, while the bond angle between of C-F-C are 145 and 119°, suggesting a small effect on the planar structures. S and Cl adsorption induces a structural deformation along the direction of plane, leading to the expansion of the lattice constant by 4.5 and 5%, respectively. The embedded B, C, Si, N, and P atoms interact with C_3N_4/C_4N_3 via sp^2-hybridization and forms three σ bonds with neighboring N atoms, resulting in no distortion in the plane of structures. The difference charge densities of the embedded atom structures are presented in Fig. 3(c) and Fig. 3(d), where blue and yellow regions represent the charge accumulation and depletion, respectively. It can be clearly seen that electrons are depleted on the atoms of C_3N_4 and C_4N_3, whereas the majority of electron enhancement is on the O and S atoms, showing charge transfer from C_3N_4 and C_4N_3 to O and S atoms.

The electronic properties of embedded H, O, S, F, Cl, B, C, Si, N, and P atoms into the holey site of C_3N_4 and C_4N_3 are investigated by analyzing the band structure, DOS and PDOS. In order to understand the modifications of the electronic properties, we investigated the new states appearing around E_F. The calculated electronic band structure are shown in Figs. 4(a,b). The majority-spin (↑) and minority-spin (↓) bands are shown by blue-lines and red-dashed lines, respectively. The embedded atoms modify the electronic states and give rise to new localized states. The H-C_3N_4 system is a direct semiconductor with a band gap of 1.82 eV in the minority ↓ spin channel, while a metallic states is found for the majority ↑ spin channel bands and induces a magnetic moment of 1 μ_B. Thus, the H-C_3N_4 structure is a spin-glass semiconductor where the ↑ spin channel is gap less, while the ↓ spin channel is semiconducting and the VBM of the↓ spin channel touches the E_F. The O-C_3N_4 system is a direct semiconductor with band gap of 2.01 eV, and transform into a p-type semiconductor after embedding. The S, B, C, Si-C_3N_4 systems become indirect semiconductors, with band gaps of 1.55, 0.93, 0.22 and 0.57 eV, respectively. The F and Cl-C_3N_4 systems exhibit a DM-SC, where the VBM and CBM are influenced by spin-splitting between the ↑ and ↓ channels

View Article Online
DOI: 10.1039/C9CP06031F

due to the magnetic C atom. The excess electrons of F and Cl atoms relative to C, leads to spin polarization and due to unpaired electrons, the F and Cl atoms attain a magnetic moment of 1 μ_B. The N and P-C_3N_4 systems show a metallic behavior. The corresponding electronic band-structures for embedded atoms in C_4N_3 are given in Fig. 4(b). The direct band gap of C_4N_3 in $\uparrow$ spin channel is narrow due to the impurity state of the embedded O, S, F, B, N and P atoms. In addition, the half-metallic character of C_4N_3 remains unchanged and induces magnetic moments in the range of 1-2 μ_B. The Cl and C-C_4N_3 systems are ferromagnetic-metals and spin-splitting occurs in the $\uparrow$ and $\downarrow$ spin channels, resulting in an induced magnetic moment of 0.3 and 1.4 μ_B, respectively. Finally, the Si-C_4N_3 structure exhibits metallic character.

The calculated DOS and PDOS for embedded H, O, S, F, Cl, B, C, N, Si and P atoms into the holey site of C_3N_4 and C_4N_3 are shown in Figs. 5(a,b). For the The H-C_3N_4 structure, the electronic states near E_F are mainly comprised of the C/N-p_z orbitals. The VBM of O, S, F, and Cl-C_3N_4 exhibit hybridization of the atoms-$p_{x,y,z}$ states with C/N-p_z states of the nearest atoms, while the CBM stems from the hybridization of O, S, F, and Cl-p_z states with C/N-p_z states of the nearest atoms. The results show nonmagnetic ground states. The embedded atom-C_3N_4 systems show asymmetrical spin splitting around the Fermi-level, implying magnetic character as shown in Fig. 5(b). The semiconductor to metal transition stems from the interaction between the embedded atoms and N atoms for the O, S, F and Cl-C_4N_3 structures. The CBM and VBM are mainly composed of states due to the hybridization of p_z orbitals. In this case, the PDOS of C, Si, N, and P-C_4N_3 indicate that the VBM and CBM of the $\uparrow$ spin channel originates from the hybridization of C, Si, N, and P-p_z and N-p_z orbitals. Interestingly, the hybridization of B-C_4N_3 is slightly different where the hybridized state near the E_F mainly originates from the B-$p_{x,y}$ orbital state in Figs. 5(a,b). The hybridization of the N/F-2p electrons and the C-2p orbitals result in a magnetic moment of 1μ_B. In the case of S, C and Si atoms, being in the same group as the C atom but having a relatively larger atomic radius, S and Si atoms distort the planar structures of C_3N_4 and C_4N_3 and increases the bond length. Our calculation show that the VB edge of C_3N_4 and C_4N_3 are not dramatically influenced by the states originating from Si-p_z orbitals appear near the CB edge,

thereby the Si-p_z orbitals are dominant in the VB edge. To investigate the spin arrangement on each atom and to further elucidate the origin of the magnetism, the difference spin density distribution is shown in the inset of Figs. 6(a-b). The magnetic moment of F-C_3N_4 occurs due to the F atom and partly from neighboring N atoms.

Embedded Li, Na, K, Be, Mg, Ca and Al atoms

The relaxed structures of embedded Li, Na, K, Be, Mg and Ca atoms into the holey site of C_3N_4 and C_4N_3, are shown in Fig. S1. Due to the stronger interaction between C_3N_4 and C_4N_3 nanosheets and embedded Li and Na yield significant distortion and results in local deformation. The DOS and PDOS of the embedded atoms show that the atoms interact through sp^2-hybridization and form three σ bonds with neighboring atoms and reconstructions can occur. The bond lengths of Li, Na, and K with nearest N atoms are in the range of $\sim$ 1.5-2.5 Å and there is a strong distortion in the planar structure which is related to the sizes of atoms. The change in the optimized structure is related to the charge transfer between the atoms and substrate. The difference charge densities are presented in Fig. S1(b). We see that the Li atom forms chemical bonds, and there is electron depletion on C_3N_4 and C_4N_3, while there is electron accumulation on the Li atom, thus charge transfer from C_3N_4 and C_4N_3 to Li. The electronic structure of embedded Li, Na, K, Be, Mg, Ca, and Al atoms are shown in Figs. 6(a,b).

It can be seen that the $\uparrow$ spin channel for Li, Na, K, and Al-C_3N_4 exhibits a metallic character, while in the $\downarrow$ spin channel, there is semiconducting character, thereby resulting in a half-metal. The calculated DOS and PDOS of Li, Na, K, Be, Mg, Ca, and Al-C_3N_4/C_4N_3 are shown in Fig. S2. The DOS of these structures exhibit difference to those of pristine C_3N_4, namely, there is an impurity state around Fermi-level. Based on the calculated PDOS, the impurity states are mainly from the hybridization of Li, Na and K *s*-orbitals with N/C-p_z states. It can be noticed that the DOS of both spin channels of these atoms are asymmetric, indicating a magnetic character with an induced magnetic moment of 1-2 μ_B. The Be- and Ca-C_3N_4 structures shows a DM-SC character and induce a magnetic moment of 2 μ_B magnetic. From the PDOS of Be-C_3N_4 we found that the

View Article Online
DOI: 10.1039/C9CP06031F

VBM and CBM originate from the hybridization of N-$p_{x,y}$ orbitals (Fig. S2).

Embedded Sc, Ti, V, Cr, Mn, Fe, Co, Ni, Cu and Zn atoms

We now consider embedding with 3*d* transition-metal (TM) atoms. The ground state structures of the embedded TM atoms are shown in Fig. S3. We found that embedded Ti, V, Mn, Fe, and Co largely retains the atomic structure, while Sc and Cr lead to a noticeable local deformation. The TM atoms bind to the three nearest N atoms and the bond lengths are in the range of 2.551-2.914Å (see Fig. S3).

The electronic structure of embedded Sc, Ti, V, Cr, Mn, Fe, Co, Ni, Cu and Zn atoms are shown in Figs. 7(a,b). We see that embedded TM atoms give rise to some localized states in the band structure, modifying the electronic properties. The ↑ spin channels in Cr, Mn, and Cu-C_3N_4 show a metallic character, while ↓ spin channels exhibit semiconductor character, whereas for Sc-C_3N_4 it is the opposite. This implies that these structures are half-metals. The half-metallic behaviour of Cu-C_3N_4 stems from the semiconducting spin channel with a 1.5 eV band gap. The magnetic moments of Sc, Cr, Mn and Cu-C_3N_4 are determined to be 1, 2, 1, and 1 μ_B, respectively. We can see for the V and Fe-C_3N_4 structures both the ↑ and ↓ spin channels are semiconducting, thus a DM-SC state can be realized with magnetic moments of 1 and 2 μ_B, respectively. These results are interesting because most of the conventional DM-SC exhibit a metallic band structure, based on embedding of atoms. The results for embedded Ti, Ni and Zn-C_3N_4 are quite different, and they exhibit semiconductor character with an indirect band gap of 0.86 eV for embedded Ti and a direct band gap for Ni and Zn of 0.85 eV and 1.2 eV, respectively. The Co-C_3N_4 becomes a DM-SC and induces a magnetic moment of 1 μ_B. The embedding of TMs into the holey site of C_3N_4 nanosheet results in defect states in the band gap and shifts the Fermi level to the conduction band. For Ti, Ni and Zn, the embedded systems retain semiconducting characteristics with significantly reduced band gap. For V, Fe and Co the systems show magnetic semiconducting characteristics due to the asymmetric spin-up and spin-down states. More interestingly, the corresponding systems for Sc, Cr, Mn and Cu exhibit half-metallic features with band gaps for one spin channel and not for

View Article Online
DOI: 10.1039/C9CP06031F

the other spin channel. Therefore, these materials with half-metallicity exhibit spin polarization, indicating that they are ideal materials for spin injection applications. The hybridization between the 3*d* orbitals of the TM and the host C_3N_4 nanosheet leads to charge transfer from the TM atoms to the C_3N_4 nanosheet (see Table 1). This transfer possibly creates a local magnetic moment on the TM atoms. The calculated total magnetic moments are 1, 1, 2, 1, 2, 1 and 1 μ_B for the embedding of Sc, V, Cr, Mn, Fe, Co and Cu atoms, respectively (see Table 1). While Ti, Ni and Zn do not show any magnetic moment.

Our results demonstrate that Sc, V, Fe and Zn-C_4N_3 induce a metal (semiconductor) character in the $\uparrow$ ($\downarrow$) spin channel, resulting in the material becoming a half-metal with a magnetic moment ranging from 1-2 μ_B. The Cr and Mn-C_4N_3 structures exhibit metallic behavior with the impurity levels crossing Fermi-level inducing magnetic moments of 0.66 and 3.8 μ_B, respectively. We find that Cu, and Co-C_3N_4 exhibit a DM-SC character. The band gaps of embedded Ni and Zn atoms are around 2 eV in the $\uparrow$ spin channel and the $\downarrow$ spin channel have magnetic moments of 3, 1, and 4 μ_B, respectively. The bonding character between TM atoms and N is indicated in the difference charge density and is shown in Figs. 7(a,b). It is clear that the TM atoms and C_3N_4/C_4N_3 nanosheets are strongly bonded due to the charge accumulation region between TM and the neighboring N atoms in many of the systems. However, it is less significant for systems such as embedded Ni and Zn atoms.

The DOS and PDOS of embedded Sc, Ti, V, Cr, Mn, Fe, Co, Ni, Cu and Zn atoms into the holey site of C_3N_4 are shown in Fig. 8. Though the TM-3*d* and TM-4*s* orbital states have similar energy values, the TM-3*d* shell is partially occupied. The TM embedded atoms induce magnetic moments to C_3N_4 and yield an exchange-splitting in TM-3*d* orbital states. The metallic state of Sc-C_3N_4 arises from the Sc-$d_{xy,yz,xz}/d_{z^2}(\downarrow)$ and N/C-$s, p_z(\downarrow)$ orbital states. The bands around E_F are mainly composed of the hybridization of Cr, Mn-$d_{xy,yz,xz}/d_{z^2}(\uparrow)$ and N/C-$p_z(\uparrow)$ orbital states for the Cr and Mn-C_3N_4. The degeneracy of majority $\uparrow$ and minority $\downarrow$ spin channels of Sc, Cr and Mn-C_3N_4 are broken and trigger magnetic moments of 1 ,2 and 1 μ_B, respectively. The V- and Fe-C_3N_4 systems become DM-semiconductors with the VBM mainly originating from the hybridization of the V-

View Article Online
DOI: 10.1039/C9CP06031F

$d_{xy,yz,xz}/d_{x^2y^2}$ (↓) orbitals with the C/N-p_z (↓) orbital, while the CBM arise due to hybridization of V-d_{xy}/d_{z^2} (↑) with C/N-p_z (↑). The Ti, Ni and Zn-C_3N_4 exhibit nonmagnetic semiconductor characer in which the VBM of Ni-C_3N_4, originates from the hybridization of Ni-$d_{xy,xz}/d_{x^2y^2}$ with N-p_z orbital states, while the CBM originates from Ni-d_{yz} with N-$p_{x,y}$ orbital states. The DOS and PDOS of embedded Sc, Ti, V, Cr, Mn, Fe, Co, Ni and Zn atoms into C_4N_3 are shown in Fig. S5. The spin-splitting can be observed around E_F for the main 3d orbital peaks in the ↑ and ↓ spin channel of the Sc, V, Fe and Zn-C_4N_3 structures. The metallic bands in ↑ or ↓ spin channels originate from the $d_{xy,yz,xz}/d_{z^2}$ and N-p_z orbital states. The Cr and Mn-C_4N_3 structures become a ferromagnetic-metal with the impurity level crossing E_F and a magnetic moment of 0.66 and 3.8 μ_B induced, respectively. The metallic band originates from Mn-$d_{xy,yz,xz}/d_{x^2-y^2}$(↑) with N-$p_{x,y}$ (↑) orbital states, while in the ↓ spin channel, the Mn-$d_{xy,yz,xz}/d_{x^2-y^2}$ orbital states are prominent. We found that the Cu, Co and Ni-C_4N_3 systems show a spin-glass semiconductor character and metallic bands near the E_F originates from hybridization of $d_{xy,yz,xz}/d_{x^2y^2}/4s$(↑) with N-$p_{x,y}$(↑) orbital states.

The difference spin density on TMs, N, and C atoms for C_3N_4 and C_4N_3 nanosheets are given in Fig. 9 (a) and Fig. 9 (b) , respectively. Figure 9(a) demonstrates the induced magnetic moments are distributed at the Sc atom and its surrounding N and C atoms. The magnetic moments couple with one another ferromagnetically. This situation also occurs for Mn and Cu (see Fig. 9 (a)). In contrast, V and Cr adsorption leads to an appreciable magnetic moment on V and Cr, together with smaller moments on neighboring N and next neighboring C atoms. The local moment on V and Cr couple with the ones on neighboring N and C atoms anti-ferromagnetically. Anti-ferromagnetic coupling is observed for Fe and Co embedding (see Fig. 9 (a)), but the magnetic moment is not localized as the cases of V and Cr. In order to better identify and investigate the effects of embedded atoms into C_3N_4 and C_4N_3, we simulated their STM images (Fig. S4). We can see that the C and N atoms appear as white spots, however, the region around O, P, Li, and Fe atoms corresponds to the brighter spot. With a bias of +2 V, the structures of embedded C_3N_4 and C_4N_3 are straightforward to identify through their STM images.

We also perform spin-orbit coupling calculations (with the GGA) for embedding of Sc, Ti, Mn, Fe and Co. The resulting electronic band structures are shown in Fig. 10 (a). We found that the embedding of Ti atom into holey site of C_3N_4 monolayer without including the SOC effect, exhibits semiconductor behavior. When including SOC, the system retains the semiconducting characteristics and the indirect band gap is about 0.34 meV. In the CBM, we can see a band splitting of about that 8 meV in the BZ due to SOC effect. The embedding of Fe and Co show magnetic semiconducting characteristics without considering SOC. With SOC, the half-metallicity of Fe changed and transformed to a semiconductor with direct band gap 0.15 eV where the VBM and CBM are located at the G-point. Without SOC, the corresponding systems for Sc, and Mn exhibit half-metallic features with one closed band gap for one spin channel and the other spin channel exhibiting a band gap. Considering the SOC effect, the system with Sc and Mn show metallic characteristic (see Fig. 10 (a)). Due to the weak screening of the Coulomb interaction in the embedded TM atom systems, we investigate the effect on the electronic structure by including the Hubbard U. Since the accurate value of U has not been determined for these systems, we investigate effects of correlation by considering a range of values for the Hubbard U term. The electronic band structure considering Hubbard U is shown in Fig. 10 (b). The correlation effects on the electronic and magnetic properties of C_3N_4 monolayer are found to be significant and cause a change of the spin polarization. The calculated total magnetic moments of Sc, Ti, Mn, Fe, and Co atoms are 1, 0, 1, 2 and 1 μ_B, respectively (see Table 1). When considering of the effect of U, the energy bands change near Fermi-level, indicating the robustness of nontrivial topology against the correlation effect in TM-3d electrons. Our results show that the magnetic moment of Sc, Ti, Mn, Fe, and Co atoms for U = 2 eV are changed to 0.2, 1.75, 1, 2.25 and 1.9 μ_B, respectively.

To understand the origin of the local magnetic moment, we consider crystal field theory and Hund rules. The local structure of the CoN_3 complex is well-known where it has the C_{3v} point symmetry; therefore, the five degenerate Co-3d orbitals are divided into a single a_1 state and two two-fold degenerate e_1 and e_2 states. The d_{xy} and $d_{x^2y^2}$ states orbitals to the e_2 states, whereas the d_{xz} and d_{yz} form e_1 states. The e_1 states are at a lower energy level than the e_2 states due

View Article Online
DOI: 10.1039/C9CP06031F

to crystal field splitting. The single degenerate a_1 state contains the d_{z^2} orbital located at the lowest energy with respect to e_1 and e_2 states. The a_1 state strongly overlaps the s-type lone pair on two-coordinated nitrogen; subsequently, they are occupied. To gain insight into magnetic properties, we first present the projected density of states (PDOS) for the C_3N_4 nanosheet with Co atom in Fig. 11(a). A large apparent spin-splitting is observed. The large exchange splitting is attributable to the intra-atomic exchange interaction due to Hund rule. The e_1 and e_2 states are nearly degenerate, that is, the two e manifolds are mixed as shown in Fig. 11(a). The a_1 state demonstrates that there is notable $p-d$ hybridization between Co and the C_3N_4 nanosheet. The a_1 state in the down-spin channel is pushed to a lower energy level relative to those of the e_1 and e_2 states due to crystal field splitting, therefore, the a_1 states are fully occupied in both spin channels; a schematic representation of electron configuration is shown in Fig. 11(b). While the Co ion (Co+1^+1) carries a local magnetic moment of about 2 μ_B, the electron injection leads unpaired electron on neighboring N and C atoms. The calculated PDOS results show that the local magnetic moment partially originates from the neighboring N atoms in the Fig. 11(a). The similar scene is true for neighboring C atom, which can be verified by the p-characterized with difference spin charge density illustrated in the Fig. 11(c). The sum of magnetic moments on neighboring N and C atoms with the Co embedding produced a total magnetic moment of 1 μ_B. The difference spin density on Co, N, and C atoms are visualized in the Fig. 11(c). We can see that the embedding of the Co atom leads to an appreciable magnitude of the magnetic moment on Co, together with slight magnitudes of moments at its first neighboring N and next neighboring C. The induced magnetic moments distributed at Co and its surrounding N and C atoms are illustrated in Fig. 11(c). The local moment on Co anti-ferromagnetically couples with the ones on neighboring N and C atoms. Taking C_3N_4 nanosheet with Co as an example, the plots of difference charge density is shown in the inset of Fig. 11(d), in which the typical ionic and covalent characteristics for C-N and Co-N bonds can be observed respectively.

View Article Online
DOI: 10.1039/C9CP06031F

Conclusion

In summary, through first-principles calculations we have explored the effects of embedded atom impurities on the structural, electronic, and magnetic properties of C_3N_4 and C_4N_3 nanosheets. Our results show that C_3N_4 is a semiconductor with direct band gap of 1.45 eV, while C_3N_4 is a half-metal. We found that the electronic properties can be effectively modified through various embedded atoms in the holey site of C_3N_4 and C_4N_3 nanosheets. The atomic structure of C_3N_4 and C_4N_3 nanosheets were found to remain intact, despite local deformations induced by the embedding of various atoms such as B, C, P, and N atoms. In contrast embedding of O, F, H, Cl and transition metal atoms results in considerable local deformations, involving bond breaking of the pristine lattices. Our results reveal that embedding H, F, Cl, Li, Na, K and Al atoms can induce magnetism into C_3N_4 nanosheet, while N and P transform the electronic structure from semiconductor to metal. The semiconductor character is preserved with embedding of O, S, B, C, and Si atoms, but interestingly they can finely tune their band gaps over a range of 0.3-2.0 eV. Be, Cl, and Mg atoms respectively, can induce a DM-SC, DM-SC and metallic character. The embedding of TM atoms into the holey site of C_3N_{34} results in defect states in the band gap and shifts the Fermi level to the conduction band. For Ti, Ni and Zn, the embedded systems retain semiconducting characteristics with significantly reduced band gap. For V, Fe and Co the systems show magnetic semiconducting characteristics due to the asymmetric spin-up and spin-down DOS. More interestingly, the corresponding systems for Sc, Cr, Mn and Cu exhibit half-metallic features with band gaps for one closed spin channel and the other opened spin channel. Embedding of H, O, S, F, B, N, P, Be, Mg and Al atoms can preserve the half-metallic nature of C_4N_3. While embedded Cl and C atoms leads to a ferromagnetic-metal, with embedding of Li, Na, K, and Ca atoms, the system becomes a metal. For embedded 3*d* TM atoms, C_4N_3 can be half-metallic for Sc, V, Fe, Ni and Zn atoms or can be transformed into a ferromagnetic-metal (with Cr and Mn), dilute-magnetic semiconductor (with Co, Cu) and a semiconductor (with Ti). Our studies further suggest that embedded nonmetal and metal atoms can be employed as effective approaches to tailor the electronic and magnetic properties of carbon nitride nanosheets, which can open alternative ways for the

View Article Online
DOI: 10.1039/C9CP06031F

application in nanoelectronics and spintronics.

Conflicts of interest

The authors declare that there are no conflicts of interest regarding the publication of this paper.

ACKNOWLEDGMENTS

This work has supported by the National Research Foundation of Korea(NRF) grant funded by the Korea government(MSIT) (NRF-2017R1A2B2011989). B. Akgenc acknowledges financial support the Kirklareli University-BAP under the Project No 189 and TUBITAK ULAKBIM, High Performance and Grid Computing Center.

View Article Online
DOI: 10.1039/C9CP06031F

Table 1: The calculated ground-state atomic, electronic and magnetic properties of embedding atoms into the holey site of C_3N_4 and C_4N_3 nanosheets: bond length between embedded-atom and its nearest neighboring atom (d_{AN}), the height of the adatom from the C_3N_4 and C_4N_3 planes (h), the electronic state (ES), as specified as metal (M), half-metal (HM), ferromagnetic-metal (FM), semiconductor (SC), and dilute-magnetic semiconductor (DM-SC),the charge transfer (ΔQ) between the embedded atom and C_3N_4 and C_4N_3 nanosheets, the magnetic moment per supercell $M_{tot}(\mu_B)$, and the initial magnetic moment of the atoms $M_{ISO}(\mu_B)$. The values in parentheses correspond to values for the C_4N_3 nanosheet.

Atom	d_{AN} (Å)	h (Å)	ES	E_g (eV)	ΔQ (e)	$M_{tot}(\mu_B)$	$M_{tot}(\mu_B)$
H	1.073 (1.086)	0 (0)	DM-SC (HM)	-	+0.266 (+0.268)	1 (3)	1
O	1.285 (1.291)	1.553 (1.293)	SC (HM)	1.05	-0.359 (-0.302)	0 (2)	2
S	1.714 (1.745)	2.029 (1.537)	SC (HM)	1.43	-0.182 (-0.109)	0 (2)	2
F	1.958 (1.416)	1.98 (1.60)	DM-SC (HM)	-	-0.207 (-0.186)	1 (3)	1
Cl	2.442 (1.759)	2.559 (2.061)	DM-SC (FM)	-	-0.099 (-0.047)	1 (0.3)	1
B	1.383 (1.404)	0 (0)	SC (HM)	0.97	+0.591 (+0.670)	0 (1)	1
C	1.343 (1.363)	0 (0)	SC (FM)	0.25	+0.689 (+0.747)	0 (1.4)	2
Si	1.577 (1.601)	0 (0)	SC (M)	0.62	+0.548 (+0.748)	0 (0)	2
N	1.365 (1.419)	0 (0)	M (HM)	-	-0.003 (-0.056)	0 (1)	3
P	1.593 (1.648)	0 (0)	M (HM)	-	-0.260 (-0.183)	0 (1)	3
Li	1.895 (1.901)	1.585 (1.599)	HM (M)	-	+0.238(+0.202)	1 (0)	1
Na	2.289 (2.255)	2.139 (2.171)	HM (M)	-	+0.457 (+0.450)	1 (0)	1
K	2.619 (2.607)	2.558 (2.574)	HM (M)	-	+0.544 (+0.554)	1 (0)	1
Be	1.573 (1.566)	0.788 (0.755)	DM-SC (HM)	-	+0.322 (+0.315)	2 (2)	0
Mg	2.067 (1.951)	1.828 (1.659)	M (HM)	-	+0.506 (+0.700)	0 (2)	0
Ca	2.266 (2.208)	2.130 (2.062)	DM-SC (M)	-	+0.664 (+0.840)	2 (0)	0
Al	1.991 (1.652)	1.706 (0)	HM (HM)	-	+0.283 (+0.789)	1 (0.3)	1
Sc	2.030 (2.001)	1.796 (1.735)	HM (HM)	-	+0.761 (+0.923)	1 (1)	1
Ti	1.923 (1.891)	1.635 (1.547)	SC (SC)	0.35 (0.12)	+0.544 (+0.639)	0 (0)	2
V	1.869 (1.833)	0.572 (1.489)	DM-SC (HM)	-	+0.331 (+0.434)	1 (1)	3
Cr	1.839 (1.815)	1.508 (1.432)	HM (FM)	-	+0.015 (+0.120)	2 (0.66)	4
Mn	1.791 (1.791)	1.377 (1.375)	HM (FM)	-	+0.981 (+1.076)	1 (3.8)	5
Fe	1.804 (1.802)	1.491 (1.485)	DM-SC (HM)	-	+0.439 (+0.567)	2 (2)	4
Co	1.812 (1.801)	1.373 (1.370)	DM-SC (DM-SC)	-	+0.350 (+0.472)	1 (1)	3
Ni	1.843 (1.848)	1.480 (1.475)	SC (HM)	0.25	+0.432(+0.530)	0 (4)	2
Cu	1.949 (1.923)	1.639 (1.595)	HM (DM-SC)	-	+0.087(+0.191)	1 (3)	1
Zn	3.408 (1.901)	3.188 (1.487)	SC (HM)	2.1	+0.245 (+0.416)	0 (2)	0

View Article Online
DOI: 10.1039/C9CP06031F

References

(1) Dong, M.; He, C.; Zhang, W. *Journal of Materials Chemistry C* **2017**, *5*, 3830–3837.

(2) Li, T.; He, C.; Zhang, W. *Applied Surface Science* **2018**, *427*, 388–395.

(3) He, C.; Zhang, J.; Zhang, W.; Li, T. *The journal of physical chemistry letters* **2019**.

(4) Zhao, G.; Cheng, Y.; Wu, Y.; Xu, X.; Hao, X. *Small* **2018**, *14*, 1704138.

(5) Zhou, Q.; Wu, M.; Zhang, M.; Xu, G.; Yao, B.; Li, C.; Shi, G. *Materials Today Energy* **2017**, *6*, 181 – 188.

(6) Lee, S. U.; Belosludov, R. V.; Mizuseki, H.; Kawazoe, Y. *Small 5*, 1769–1775.

(7) Li, J.; Cui, W.; Sun, Y.; Chu, Y.; Cen, W.; Dong, F. *J. Mater. Chem. A* **2017**, *5*, 9358–9364.

(8) Zheng, Y.; Liu, J.; Liang, J.; Jaroniec, M.; Qiao, S. Z. *Energy Environ. Sci.* **2012**, *5*, 6717–6731.

(9) Zhu, G.; LÃij, K.; Sun, Q.; Kawazoe, Y.; Jena, P. *Computational Materials Science* **2014**, *81*, 275 – 279.

(10) Li, X.; Zhang, S.; Wang, Q. *Phys. Chem. Chem. Phys.* **2013**, *15*, 7142–7146.

(11) Mannix, A. J., K. B. H. M. C. G. N. P. *Nature Reviews Chemistry* **2017**, *1*, 0014.

(12) Du, A.; Sanvito, S.; Smith, S. C. *Phys. Rev. Lett.* **2012**, *108*, 197207.

(13) Hu Tao,; Hashmi Arqum,; Hong Jisang, *Scientific Reports* **2014**, *4*, 6059.

(14) Hashmi Arqum,; Hong Jisang, *Scientific Reports* **2014**, *4*, 4374.

(15) Zhang, X.; Zhao, M.; Wang, A.; Wang, X.; Du, A. *J. Mater. Chem. C* **2013**, *1*, 6265–6270.

(16) Yndurain, F. *Phys. Rev. B* **2014**, *90*, 245420.

View Article Online
DOI: 10.1039/C9CP06031F

(17) Nair R.R.,; Tsai I.-L.,; Sepioni M.,; Lehtinen O.,; Keinonen J.,; Krasheninnikov A.V.; Castro Neto A.H.,; Katsnelson M.I.,; Geim A.K.,; Grigorieva I.V., *Nature Communications* **2013**, *4*, 2010.

(18) König, M.; Wiedmann, S.; Brüne, C.; Roth, A.; Buhmann, H.; Molenkamp, L. W.; Qi, X.-L.; Zhang, S.-C. *Science* **2007**, *318*, 766–770.

(19) Liu, C.-X.; Qi, X.-L.; Dai, X.; Fang, Z.; Zhang, S.-C. *Physical review letters* **2008**, *101*, 146802.

(20) Kaloni, T. P.; Singh, N.; Schwingenschlögl, U. *Physical Review B* **2014**, *89*, 035409.

(21) Ezawa, M. *Physical review letters* **2012**, *109*, 055502.

(22) Yu, R.; Zhang, W.; Zhang, H.-J.; Zhang, S.-C.; Dai, X.; Fang, Z. *Science* **2010**, *329*, 61–64.

(23) Lin, X.; Ni, J. *Physical Review B* **2012**, *86*, 075440.

(24) Kaloni, T. P.; Chang, K.; Miller, B. J.; Xue, Q.-K.; Chen, X.; Ji, S.-H.; Parkin, S. S.; Barraza-Lopez, S. *Physical Review B* **2019**, *99*, 134108.

(25) Chang, K.; Kaloni, T. P.; Lin, H.; Bedoya-Pinto, A.; Pandeya, A. K.; Kostanovskiy, I.; Zhao, K.; Zhong, Y.; Hu, X.; Xue, Q.-K. et al. *Advanced Materials* **2019**, *31*, 1804428.

(26) Li, T.; He, C.; Zhang, W. *J. Mater. Chem. A* **2019**, *7*, 4134–4144.

(27) Kaloni, T. P. *The Journal of Physical Chemistry C* **2014**, *118*, 25200–25208.

(28) Bafekry, A.; Stampfl, C.; Ghergherehchi, M.; Shayesteh, S. F. *Carbon* **2020**, *157*, 371 – 384.

(29) Akgenc, B. *Computational Materials Science* **2020**, *171*, 109231.

(30) Kahraman, Z.; Kandemir, A.; Yagmurcukardes, M.; Sahin, H. *The Journal of Physical Chemistry C* **2019**, *123*, 4549–4557.

(31) Bafekry, A.; Stampfl, C.; Shayesteh, s. *ChemPhysChem n/a*, .

(32) Mortazavi, B.; Shahrokhi, M.; Madjet, M. E.; Hussain, T.; Zhuang, X.; Rabczuk, T. *J. Mater. Chem. C* **2019**, *7*, 3025–3036.

(33) Akgenc, B. *Solid State Communications* **2019**, *303-304*, 113739.

(34) Bafekry, A.; Akgenc, B.; Shayesteh, S. F.; Mortazavi, B. *Applied Surface Science* **2019**, 144450.

(35) Mortazavi, B.; Madjet, M. E.; Shahrokhi, M.; Ahzi, S.; Zhuang, X.; Rabczuk, T. *Carbon* **2019**, *147*, 377 – 384.

(36) Yagmurcukardes, M.; Ozen, S.; Iyikanat, F.; Peeters, F.; Sahin, H. *Physical Review B* **2019**, *99*, 205405.

(37) Bafekry, A.; Stampfl, C.; Shayesteh, S. F.; Peeters, F. M. *Advanced Electronic Materials n/a*, 1900459.

(38) Kiymaz, D.; Yagmurcukardes, M.; Tomak, A.; Sahin, H.; Senger, R. T.; Peeters, F. M.; Zareie, H. M.; Zafer, C. *Nanotechnology* **2016**, *27*, 455604.

(39) Akgenc, B. *Journal of Materials Science* **2019**, *54*, 9543–9552.

(40) Mortazavi, B.; Shahrokhi, M.; Zhuang, X.; Rabczuk, T. *J. Mater. Chem. A* **2018**, *6*, 11022–11036.

(41) Bafekry, A.; Farjami Shayesteh, S.; Ghergherehchi, M.; Peeters, F. M. *Journal of Applied Physics* **2019**, *126*, 144304.

(42) Akgenc, B.; Kinaci, A.; Tasseven, C.; Cagin, T. *Materials Chemistry and Physics* **2018**, *205*, 315 – 324.

(43) Mortazavi, B.; Makaremi, M.; Shahrokhi, M.; Fan, Z.; Rabczuk, T. *Carbon* **2018**, *137*, 57 – 67.

View Article Online
DOI: 10.1039/C9CP06031F

(44) Bafekry, A.; Mortazavi, B.; Shayesteh, S. F. *Journal of Magnetism and Magnetic Materials* **2019**, *491*, 165565.

(45) Mortazavi, B.; Shahrokhi, M.; Madjet, M. E.; Makaremi, M.; Ahzi, S.; Rabczuk, T. *Carbon* **2019**, *141*, 291 – 303.

(46) Chan, K. T.; Neaton, J. B.; Cohen, M. L. *Phys. Rev. B* **2008**, *77*, 235430.

(47) Sahin, H.; Peeters, F. M. *Phys. Rev. B* **2013**, *87*, 085423.

(48) Bafekry, A. *Physica E: Low-dimensional Systems and Nanostructures* **2019**.

(49) Pang, Q.; Li, L.; li Zhang, L.; ling Zhang, C.; ling Song, Y. *Canadian Journal of Physics* **2015**, *93*, 1310–1318.

(50) Li, Y.; Xia, C.; Du, J.; Xiong, W.; Li, X.; Wei, S. *Phys. Chem. Chem. Phys.* **2017**, *19*, 5423–5429.

(51) Lalitha, M.; Mahadevan, S. S.; Lakshmipathi, S. *Journal of Materials Science* **2017**, *52*, 815–831.

(52) Sun, M.; Wang, S.; Du, Y.; Yu, J.; Tang, W. *Applied Surface Science* **2016**, *389*, 594 – 600.

(53) Sun, M.; Ren, Q.; Wang, S.; Zhang, Y.; Du, Y.; Yu, J.; Tang, W. *Computational Materials Science* **2016**, *118*, 112 – 116.

(54) Cheng, Y. C.; Zhu, Z. Y.; Mi, W. B.; Guo, Z. B.; Schwingenschlögl, U. *Phys. Rev. B* **2013**, *87*, 100401.

(55) Sun, M.; Ren, Q.; Zhao, Y.; Wang, S.; Yu, J.; Tang, W. *Journal of Applied Physics* **2016**, *119*, 143904.

(56) ÃIJzengi AktÃijrk, O.; Tomak, M. *Applied Surface Science* **2011**, *258*, 800 – 805.

(57) Gao, S.; Ren, Z.; Wan, L.; Zheng, J.; Guo, P.; Zhou, Y. *Applied Surface Science* **2011**, 257, 7443 – 7446.

(58) Bafekry, A.; Farjami Shayesteh, S.; Peeters, F. M. *Phys. Chem. Chem. Phys.* **2019**, *21*, 21070–21083.

(59) Xue, Y.; Liu, J.; Chen, H.; Wang, R.; Li, D.; Qu, J.; Dai, L. *Angewandte Chemie International Edition 51*, 12124–12127.

(60) Roy-Mayhew, J. D.; Bozym, D. J.; Punckt, C.; Aksay, I. A. *ACS Nano* **2010**, *4*, 6203–6211.

(61) Ganji, M. D.; Sharifi, N.; Ardjmand, M.; Ahangari, M. G. *Applied Surface Science* **2012**, *261*, 697 – 704.

(62) Bafekry, A.; Ghergherehchi, M.; Farjami Shayesteh, S. *Phys. Chem. Chem. Phys.* **2019**, *21*, 10552–10566.

(63) Lee, Y.; Lee, S.; Hwang, Y.; Chung, Y.-C. *Applied Surface Science* **2014**, *289*, 445 – 449.

(64) Khan, I.; Hong, J. *New Journal of Physics* **2015**, *17*, 023056.

(65) Bafekry, A.; Ghergherehchi, M.; Shayesteh, S. F.; Peeters, F. *Chemical Physics* **2019**, *526*, 110442.

(66) Seixas, L.; Carvalho, A.; Castro Neto, A. H. *Phys. Rev. B* **2015**, *91*, 155138.

(67) Ramasubramaniam, A.; Naveh, D. *Phys. Rev. B* **2013**, *87*, 195201.

(68) Tagani, M. B. *Journal of Magnetism and Magnetic Materials* **2020**, *497*, 166027.

(69) Tagani, M. B. *Computational Materials Science* **2018**, *153*, 126 – 133.

(70) Bafekry, A.; Shayesteh, S. F.; Peeters, F. *The Journal of Physical Chemistry C* **2019**, *123*, 12485–12499.

(71) Hu, A.-M.; Luo, H.-J.; Xiao, W.-Z. *Journal of Magnetism and Magnetic Materials* **2020**, *493*, 165745.

(72) Izadi Vishkayi, S.; Bagheri Tagani, M. *Phys. Chem. Chem. Phys.* **2018**, *20*, 10493–10501.

(73) Bafekry, A.; Shayesteh, S. F.; Peeters, F. M. *Journal of Applied Physics* **2019**, *126*, 215104.

(74) Perdew, J. P.; Burke, K.; Ernzerhof, M. *Phys. Rev. Lett.* **1996**, *77*, 3865–3868.

(75) Troullier, N.; Martins, J. L. *Phys. Rev. B* **1991**, *43*, 1993–2006.

(76) Ozaki, T. *Phys. Rev. B* **2003**, *67*, 155108.

(77) Ozaki, T.; Kino, H. *Phys. Rev. B* **2004**, *69*, 195113.

(78) Monkhorst, H. J.; Pack, J. D. *Phys. Rev. B* **1976**, *13*, 5188–5192.

(79) Tersoff, J.; Hamann, D. R. *Phys. Rev. Lett.* **1983**, *50*, 1998–2001.

(80) Horcas, I.; FernÃąndez, R.; GÃşmez-RodrÃguez, J. M.; Colchero, J.; GÃşmez-Herrero, J.; Baro, A. M. *Review of Scientific Instruments* **2007**, *78*, 013705.

(81) Mulliken, R. S. *The Journal of Chemical Physics* **1955**, *23*, 2343–2346.

(82) Kroke, E.; Schwarz, M.; Horath-Bordon, E.; Kroll, P.; Noll, B.; Norman, A. D. *New J. Chem.* **2002**, *26*, 508–512.

View Article Online
DOI: 10.1039/C9CP06031F

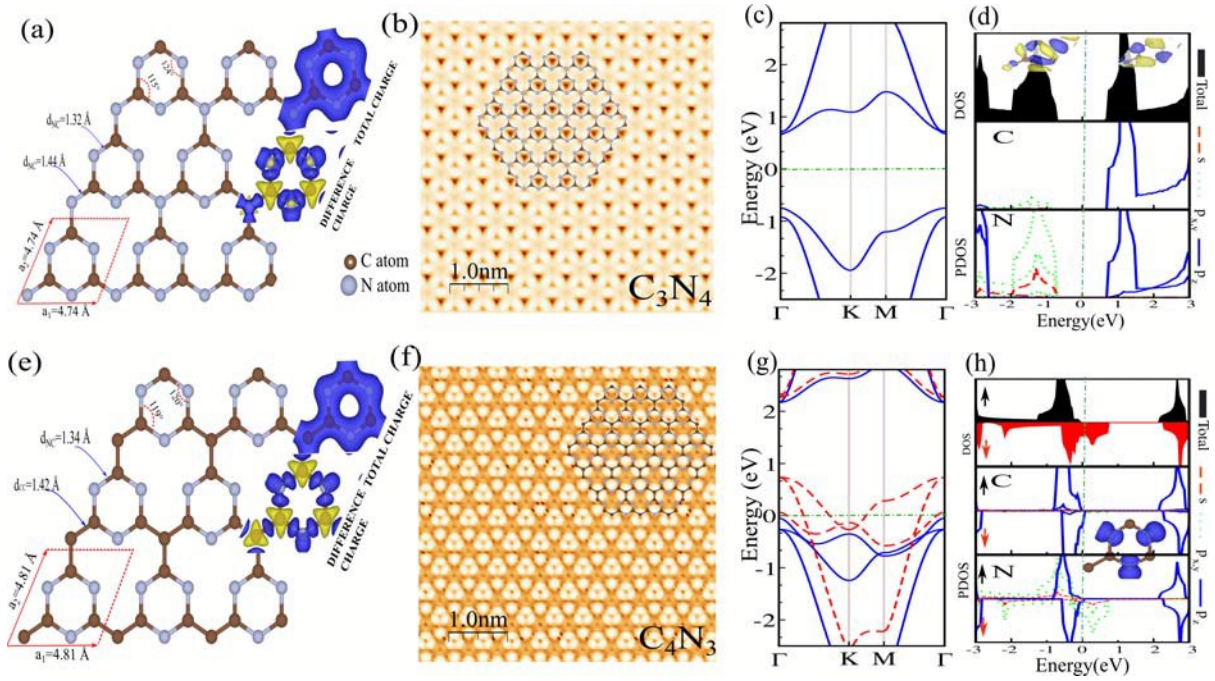

Figure 1: (a,e) Geometric structures, (b,f) simulated STM images, (c,g) calculated electronic-band structure, (d,h) density of states (DOS) and partial DOS (PDOS) of C_3N_4 and C_4N_3 nanosheets. The primitive unit cell is indicated by a red parallelogram in (a) and (e). C and N atoms are represented by brown and blue balls, respectively. The total charge density and charge difference densities are also indicated in the same panels. The charge accumulation and depletion are shown by the blue and yellow regions, respectively. The STM images are overlaid with their corresponding structures, with the brown atoms representing C and the blue atoms representing N. The charge densities of valance band minimum (VBM) and conduction band maximum (CBM) are indicated as insets. The zero of energy is set to Fermi-level (E_F), as shown by the green dash-point line.

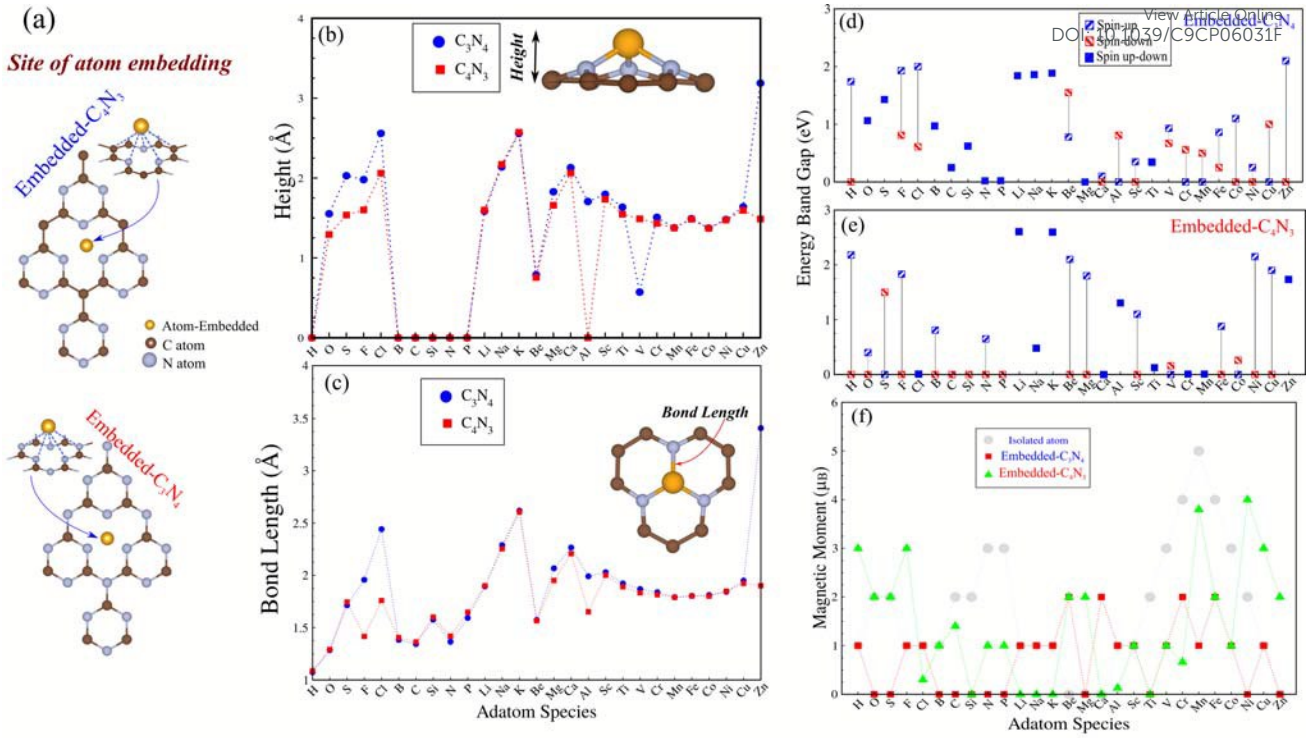

Figure 2: (a) Schematic atomic structure for embedded atoms into C_3N_4 (above) and C_4N_3 (below). (b,c) The calculated ground-state structural parameters, which include bond length and height for different embedded atoms in C_3N_4 and C_4N_3. The schematic geometry of the embedded atom into holey site of C_3N_4 and C_4N_3 nanosheets is indicated in the same panel. The variation of (d,e) the band gap and (f) the magnetic moment for difference species of atoms.

View Article Online
DOI: 10.1039/C9CP06031F

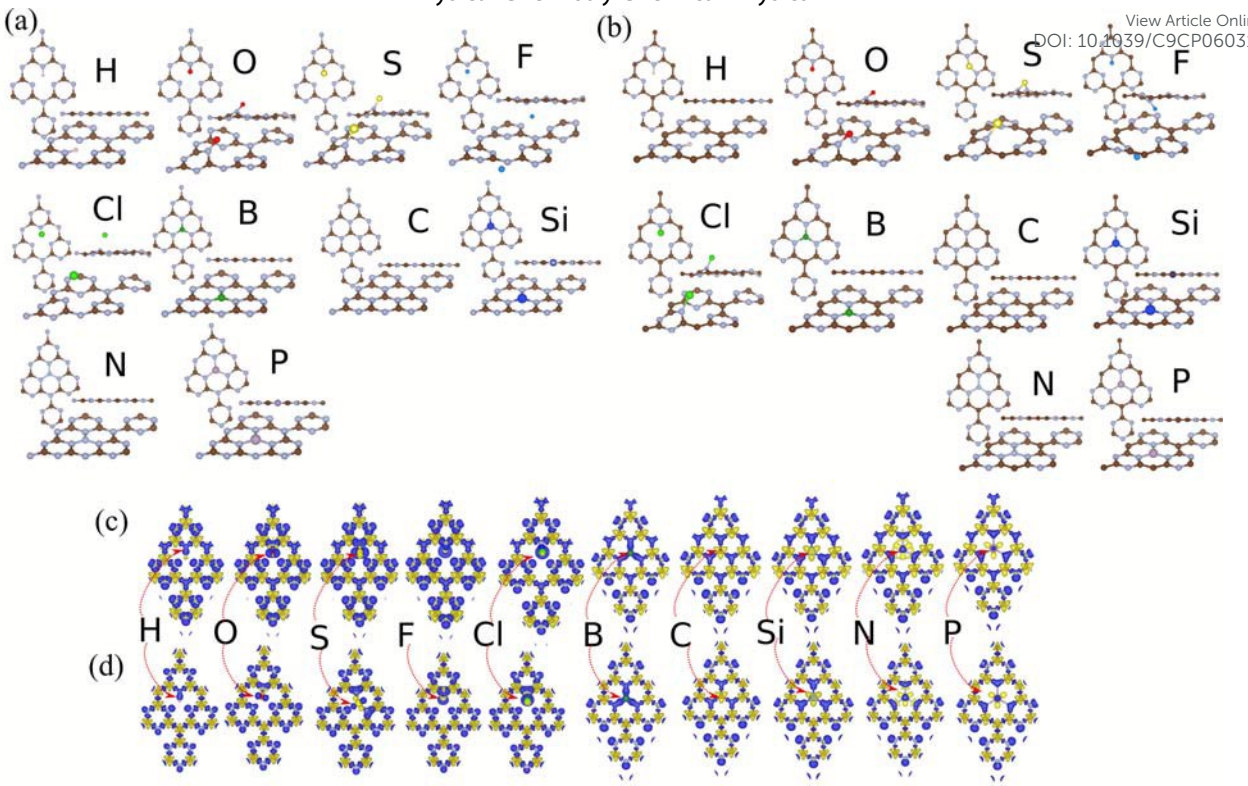

Figure 3: Top, side and perspective views of optimized structures of embedded H, O, S, F, Cl, B, C, Si, N, and P atoms into the holey site of (a) C_3N_4 and (b) C_4N_3 nanosheets. Difference charge densities of embedded atoms into (c) C_3N_4 and (d) C_4N_3 nanosheets. The charge accumulation and depletion are shown by color scheme with blue and yellow regions represent, respectively.

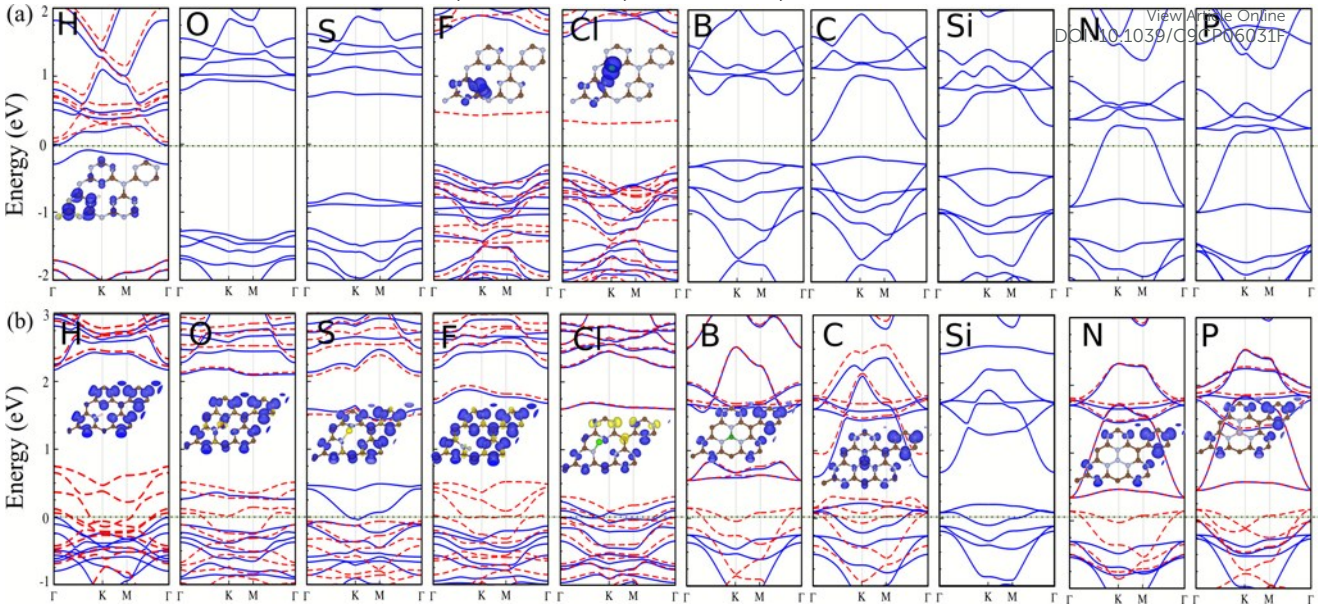

Figure 4: Electronic structure of embedded H, O, S, F, Cl, B, C, N, Si and P atoms into the holey site of (a) C_3N_4 and (b) C_4N_3 nanosheets. Difference spin density is shown in the inset. The majority (↑) and minority(↓) spin directions represent blue and yellow regions, respectively. The zero of energy is set to Fermi-level, shown by the green dash-point line.

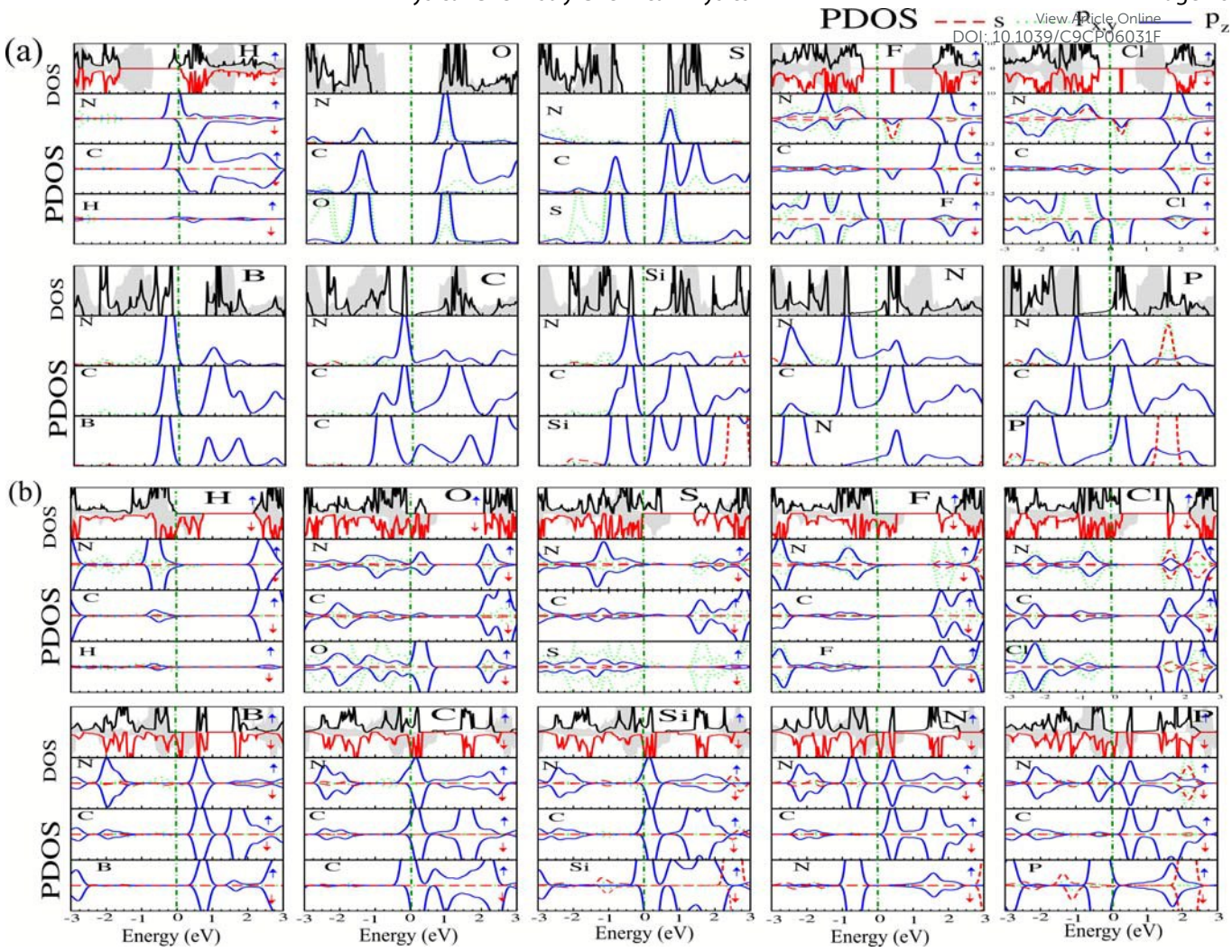

Figure 5: DOS and PDOS of s, $p_{x,y}$, and p_z orbitals for embedded H, O, S, F, Cl, B, C, N, Si and P atoms into the holey site of (a) C_3N_4 and (b) C_4N_3 nanosheets. Difference spin density is shown in the inset. The majority (↑) and minority(↓) spin directions represent blue and yellow regions, respectively. The zero of energy is set to Fermi-level, shown by the green dash-point line.

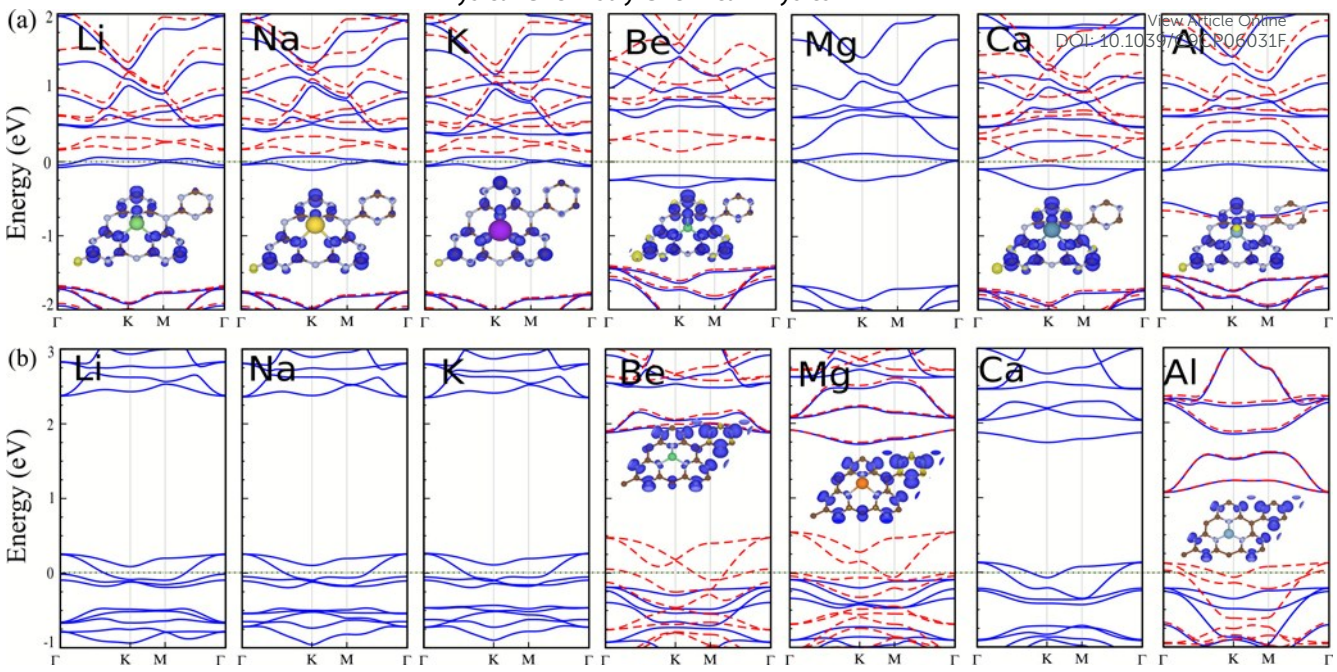

Figure 6: (a) Electronic structure of embedded Li, Na, K, Be, Mg, Ca, and Al atoms into the holey site of (a) C_3N_4 and (b) C_4N_3 nanosheets. Difference spin density is shown in the inset. The majority (↑) and minority(↓) spin directions represent blue and yellow regions, respectively. The zero of energy is set to E_F, shown by the green dash-point line.

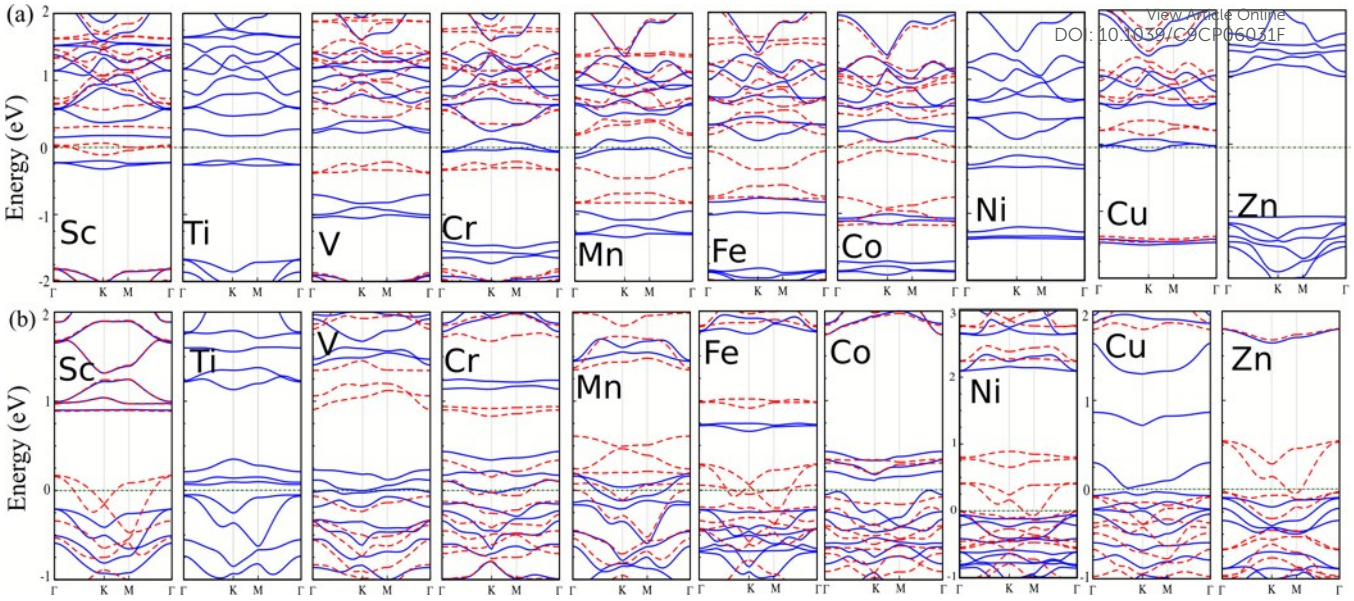

Figure 7: (a) Electronic band structure of embedded Sc, Ti, V, Cr, Mn, Fe, Co, Ni and Zn atoms into the holey site of (a) C_3N_4 and (b) C_4N_3 nanosheets. Difference spin density is shown in the inset. The majority (↑) and minority(↓) spin directions represent blue and yellow regions, respectively. The zero of energy is set to Fermi-level, shown by the green dash-point line.

View Article Online
DOI: 10.1039/C9CP06054F

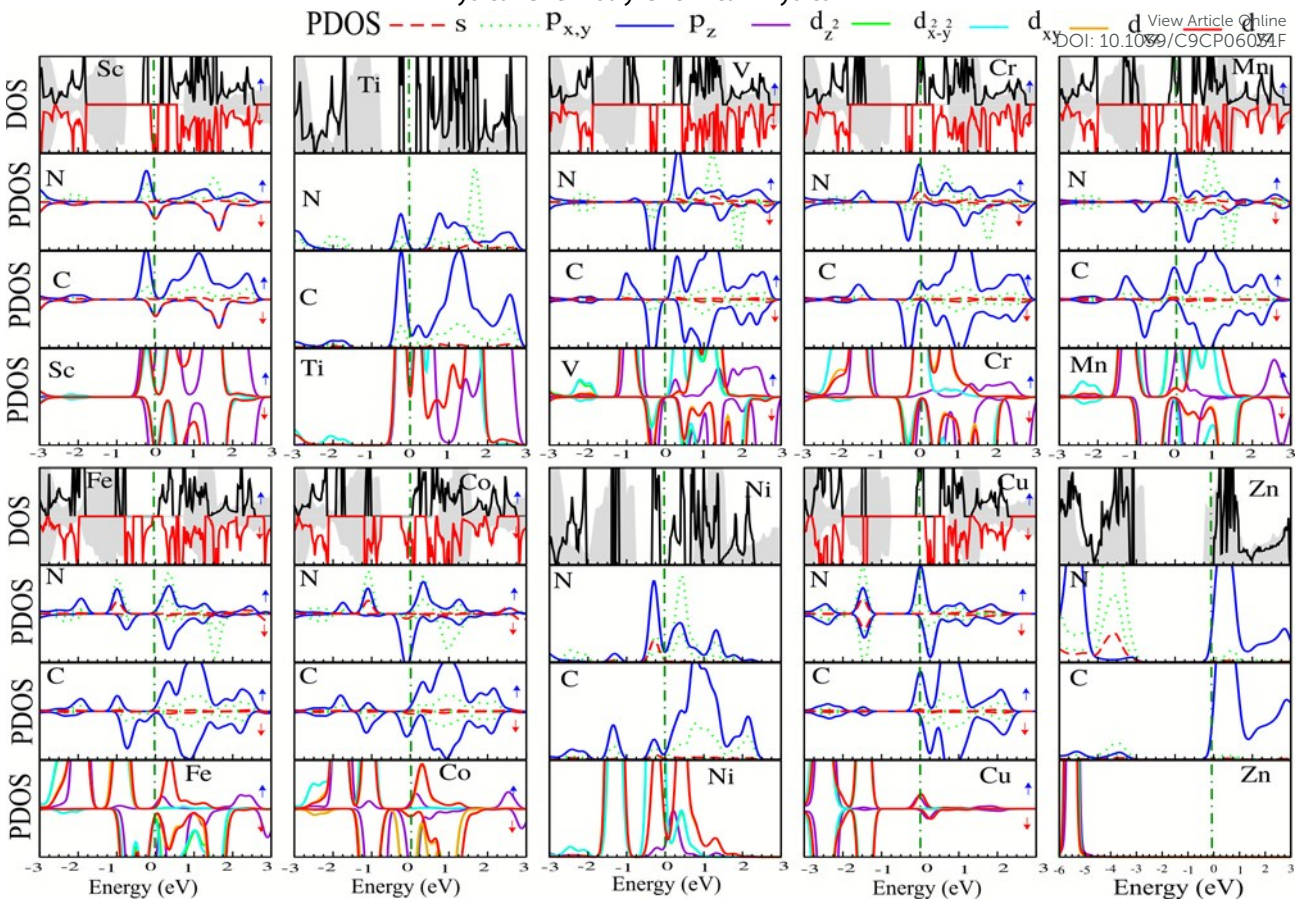

Figure 8: DOS and PDOS of s, $p_{x,y}$, p_z, d_{z^2}, $d_{x^2y^2}$, d_{xy}, d_{yz}, and d_{xz} orbitals for embedded Sc, Ti, V, Cr, Mn, Fe, Co, Ni, Cu and Zn atoms into the holey site of C_3N_4 nanosheet. The zero of energy is set to Fermi-level, shown by the vertical green dash-point line.

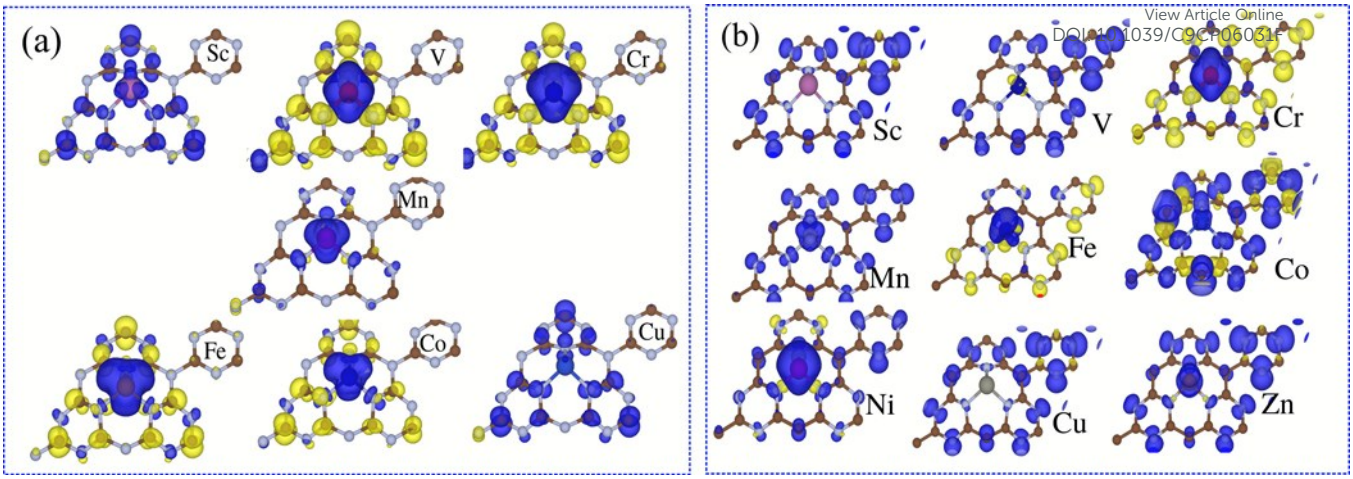

Figure 9: (a) Difference spin density for embedded TM atoms into the holey site of (a) C_3N_4 and (b) C_4N_3 nanosheets. The majority (↑) and minority (↓) spin directions represent blue and yellow regions, respectively.

Physical Chemistry Chemical Physics

View Article Online
DOI: 10.1039/C9CP06031F

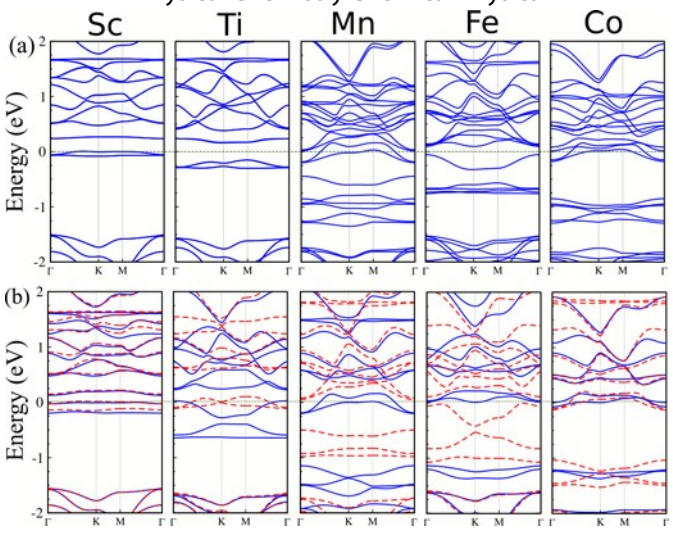

Figure 10: Electronic band structure of embedded Sc, Ti, Mn, Fe and Co atoms into the holey site of C_3N_4 nanosheet (a) with considerÄśng of spin orbital coupling (SOC) effect and (b) Hubbard U. The zero of energy is set to Fermi-level, shown by the green dash-point line.

View Article Online
DOI: 10.1039/C9CP06031F

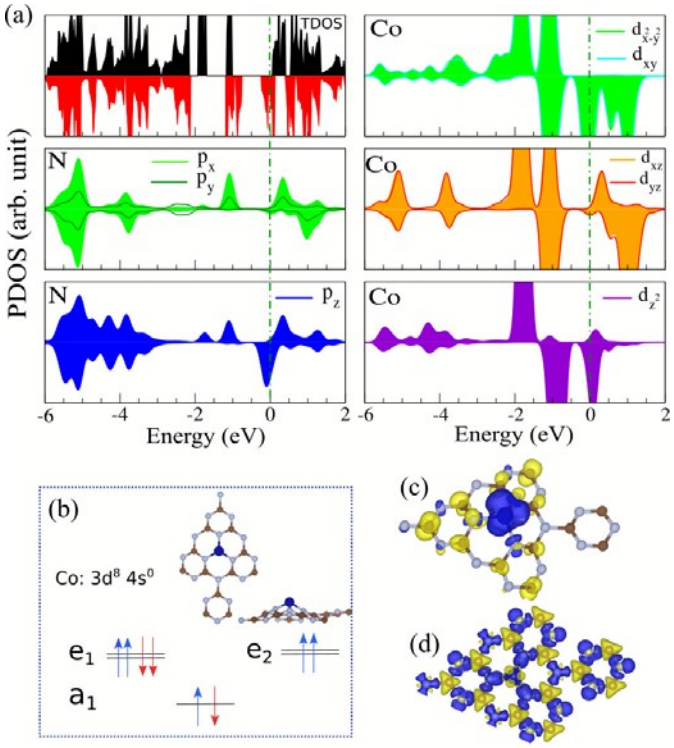

Figure 11: (a) PDOS of Co-3*d* and three N atoms surrounding Co, (b) Schematic of the occupation of electrons under crystal field for C_3N_4 embedded by Co atom. (c) Differnece spin density is shown in the inset. The majority (↑) and minority (↓) spin directions represent blue and yellow regions, respectively. The optimized structure of C_3N_4 embedded with the Co atom indicated in the same panel. (d) Difference charge density is shown where the blue and yellow regions represent charge accumulation and depletion, respectively.